



# The effect of carbon concentration on its core-mantle partitioning behavior in inner Solar System rocky bodies

Damanveer S. Grewal\*, Rajdeep Dasgupta, Sanath Aithala

Department of Earth, Environmental, and Planetary Sciences, Rice University, 6100 Main Street, MS 126, Houston, TX 77005, USA



## ARTICLE INFO

### Article history:

Received 11 January 2021

Received in revised form 25 June 2021

Accepted 26 June 2021

Available online xxxx

Editor: J. Badro

### Keywords:

carbon

metal-silicate carbon partitioning

core-mantle differentiation

volatile depletion

## ABSTRACT

Partitioning of carbon (C) into the cores of rocky protoplanets and planets is one of the primary causes of its depletion in their bulk silicate reservoirs. Most of the experimental studies that determined the alloy to silicate melt partition coefficient of carbon ( $D_C^{\text{alloy/silicate}}$ ) have been conducted in graphite-saturated conditions. Because carbon is a minor element in all known protoplanetary and planetary cores, it is not known whether graphite-saturated  $D_C^{\text{alloy/silicate}}$  values are applicable to core-mantle differentiation in rocky bodies which likely occurred in C-poor conditions. In this study we experimentally determined  $D_C^{\text{alloy/silicate}}$  in MgO capsules with variable bulk C contents between oxygen fugacity ( $fO_2$ ) of IW-6.35 and IW-2.59 at a fixed  $P$  (3 GPa)- $T$  (1700°C). A mafic-ultramafic (NBO/T = 1.23-1.72) and mildly hydrous (bulk H = 44-161 ppm) nature of the silicate melts caused anhydrous C species ( $CO_3^{2-} + CO$ ) to dominate over a wider  $fO_2$  range (>IW-4.2) in comparison to previous studies. This resulted in an increase in  $D_C^{\text{alloy/silicate}}$  with decreasing  $fO_2$  from IW-2.6 to IW-4.2 followed by a drop at more reduced conditions due to the formation of C-H species. Importantly,  $D_C^{\text{alloy/silicate}}$  increases with increasing bulk C content of the system at a given  $fO_2$ . Partitioning of C between alloy and silicate melts follows non-Henrian behavior (i.e., it depends on bulk C content) because the activity coefficient of C in the alloy melt ( $\gamma_C^{\text{alloy melt}}$ ) varies with C content in the alloy. Therefore, in addition to other intensive ( $P$ ,  $T$ ,  $fO_2$ ) and extensive variables (alloy and silicate melt compositions),  $D_C^{\text{alloy/silicate}}$  also depends on the bulk C content available during core-mantle differentiation. Consequently, previously determined  $D_C^{\text{alloy/silicate}}$  for C-rich alloys are not directly applicable for core-mantle differentiation in relatively C-poor magma oceans (MOs). Because the experiments from the present study more realistically simulate C-poor cores and mildly hydrous, mafic-ultramafic silicate MOs, our data can be used to more accurately predict C fractionation between MOs and cores in inner Solar System rocky bodies. Our study suggests that closed system MO-core equilibration should have led to less severe depletion of C in the silicate reservoirs of inner Solar System rocky bodies than previously predicted.

© 2021 Elsevier B.V. All rights reserved.

## 1. Introduction

Metal-silicate separation is one of the primary differentiation processes that can fractionate carbon (C) from the silicate reservoirs of rocky bodies during their growth (e.g., Dasgupta and Grewal, 2019; Kuramoto and Matsui, 1996; Wood, 1993). Relevant data pertaining to C fractionation during core-mantle differentiation in shallow ( $\leq 8$  GPa) and deep MOs ( $> 8$  GPa) have been generated in multiple high pressure ( $P$ )-temperature ( $T$ ) experimental studies over the last decade (Armstrong et al., 2015; Blanchard et al., 2019; Chi et al., 2014; Dalou et al., 2017; Dasgupta et al., 2013;

Fichtner et al., 2021; Fischer et al., 2020; Grewal et al., 2019b; Kuwahara et al., 2021, 2019; Li et al., 2016, 2015; Malavergne et al., 2019; Stanley et al., 2014; Tsuno et al., 2018). The effects of  $P$ ,  $T$ ,  $fO_2$  (oxygen fugacity), NBO/T (a measure of degree of silicate melt polymerization and expressed as total non-bridging oxygens per tetrahedral cations;  $NBO/T = (2 \times \text{Total O})/T - 4$ , where  $T = \text{Si} + \text{Ti} + \text{Al} + \text{Cr} + \text{P}$ ), and alloy melt composition (S and Si content of the alloy) on  $D_C^{\text{alloy/silicate}}$  in the presence or absence of other major volatiles like nitrogen (N) and water have been studied extensively. Experimentally determined  $D_C^{\text{alloy/silicate}}$  in the range of  $\sim 1$ -10,000 (with most values being  $\gg 1$ ) suggest C should have efficiently partitioned into protoplanetary and planetary cores.

Partitioning experiments between alloy and silicate melts in large volume presses are typically conducted in MgO or graphite

\* Corresponding author.

E-mail address: dsg10@rice.edu (D.S. Grewal).

**Table 1**

Summary of experimental conditions, resulting assemblage, oxygen fugacity, and alloy-silicate partition coefficient of carbon (C).

Exp No.	P (GPa)	T (°C)	a Duration (h)	Capsule	b Starting composition	Assemblage	log $fO_2$ ( $\Delta IW$ )		$D_C^{\text{alloy/silicate}}$	$1 - \sigma$
							c Ideal	d Non-ideal		
*G644	3	1700	1.5	MgO	70%Thb1+30%Fe-5Ni-0C-7.5Si	Periclase+Silicate Melt+Alloy Melt	−3.04	−2.83	837	208
*X75	3	1700	1.5	MgO	70%Thb1+30%Fe-5Ni-1C-7.5Si	Periclase+Silicate Melt+Alloy Melt	−2.99	−2.71	1312	232
*G641	3	1700	1.5	MgO	70%Thb1+30%Fe-5Ni-2C-7.5Si	Periclase+Silicate Melt+Alloy Melt	−2.86	−2.59	1820	254
*G635	3	1700	0.5	MgO	70%Thb1+30%Fe-5Ni-0C-12.5Si	Periclase+Silicate Melt+Alloy Melt	−4.78	−4.47	3463	1379
*X72	3	1700	2	MgO	70%Thb1+30%Fe-5Ni-0C-12.5Si	Periclase+Silicate Melt+Alloy Melt	−4.54	−4.21	2935	623
*G636	3	1700	6	MgO	70%Thb1+30%Fe-5Ni-0C-12.5Si	Periclase+Silicate Melt+Alloy Melt	−4.59	−4.25	3355	577
*G637	3	1700	12	MgO	70%Thb1+30%Fe-5Ni-0C-12.5Si	Periclase+Silicate Melt+Alloy Melt	−4.61	−4.30	2553	609
*G640	3	1700	1.5	MgO	70%Thb1+30%Fe-5Ni-1C-12.5Si	Periclase+Silicate Melt+Alloy Melt	−4.51	−4.36	5755	560
*G642	3	1700	1.5	MgO	70%Thb1+30%Fe-5Ni-2C-12.5Si	Periclase+Olivine+Silicate Melt+Alloy Melt	−4.48	−4.30	8045	888
G648	3	1700	1.5	MgO	70%Thb1+30%Fe-5Ni-0C-12.5Si	Periclase+Silicate Melt+Alloy Melt	−5.65	−5.35	1090	257
B480	3	1700	1.5	MgO	70%Thb1+30%Fe-5Ni-1C-17.5Si	Periclase+Silicate Melt+Alloy Melt	−5.58	−5.25	1680	511
*B482	3	1700	1.5	MgO	70%Thb1+30%Fe-5Ni-2C-17.5Si	Periclase+Silicate Melt+Alloy Melt	−5.50	−5.44	2521	121
X85	3	1700	1.5	MgO	70%Thb1+30%Fe-5Ni-0C-22.5Si	Periclase+Olivine+Silicate Melt+Alloy Melt	−6.67	−6.35	1803	338
B481	3	1700	1.5	MgO	70%Thb1+30%Fe-5Ni-1C-22.5Si	Periclase+Silicate Melt+Alloy Melt	−6.66	−6.32	1469	256
B483	3	1700	1.5	MgO	70%Thb1+30%Fe-5Ni-2C-22.5Si	Periclase+Silicate Melt+Alloy Melt	−6.51	−6.18	1901	371

Experimental numbers marked by \* produced silicate melt pool comprising both a dendritic matte and a glassy domain. For the other experiments, the silicate melt pools were entirely glassy.

a The experiments were held at 850–900 °C for 2–12 h before raising to the target temperature in order to reduce the porosity of MgO capsules and prevent the leakage of silicate melt and alloy melt.

b For details see Supplementary Table 1.

c  $fO_2$  with respect to iron-wüstite buffer ( $\Delta IW$ ) calculated using ideal solution model for both alloy and silicate melts.

d  $fO_2$  with respect to iron-wüstite buffer ( $\Delta IW$ ) calculated using non-ideal solution model for both alloy and silicate melts (see text for details).

$fO_2$  calculations are made using the average FeO and Fe contents of silicate melts and alloys, respectively.

e  $1 - \sigma$  error for  $D_C^{\text{alloy/silicate}}$  is obtained by propagating  $1 - \sigma$  standard deviation error on C content in the alloy and silicate melt.

capsules. Silicate melts in MgO capsules transform into more depolymerized compositions (or higher NBO/T) relative to their starting compositions due to reaction with capsule walls at high  $T$  (e.g., Kilburn and Wood, 1997). Whereas the silicate melt compositions remain effectively unchanged in relatively inert graphite capsules. As the probability of quenching large homogeneous, glassy pools using more polymerized silicate melts is high (a requirement to reliably determine C concentration in silicate melts via SIMS (Dasgupta et al., 2013)), most of the experiments to determine  $D_C^{\text{alloy/silicate}}$  have been conducted in graphite capsules. This leads to a crucial experimental artifact – graphite-saturated nature of both alloy and silicate melts, with Fe,Ni-alloys (S-, Si- and N-free) containing extremely high amounts of C (~5–8 wt.%) (e.g., Dasgupta et al., 2013). However, the amount of C available during core-mantle differentiation in the MOs of inner Solar System rocky bodies may not have been high enough to form graphite-saturated alloys (Keppler and Golabek, 2019). Planets with likely S-rich (e.g., Mars; e.g., Brennan et al., 2020) or Si-rich (e.g., Mercury; e.g., Cartier and Wood, 2019) cores could have been the exception as C solubility in such alloy melts is low (<1 wt.%; Grewal et al., 2019b; Li et al., 2016; Tsuno et al., 2018). Due to a large density difference between metallic and silicate melts, it is expected that the metal droplets should rapidly sink to the core without drawing out substantial amount of C from the atmosphere-MO system (Hirschmann, 2012; Keppler and Golabek, 2019). Consequently, the amount of C partitioned into the core forming alloy melts must have been well-below their C saturation limit (for realistic alloy-silicate mass ratios and bulk C contents). Indeed, C, analogous to other major volatiles like N (Grewal et al., 2021b), is a trace element in magmatic iron meteorites (the only known representative of protoplanetary cores) (Hirschmann et al., 2021). Geophysical and geochemical considerations also point towards C content of the present-day Earth's outer core being well below its saturation limit, i.e., typically not exceeding 0.2–2 wt.% C (e.g., Badro et al., 2015; Bajgain et al., 2021; Wood et al., 2013).

Due to a paucity of  $D_C^{\text{alloy/silicate}}$  data in graphite-undersaturated conditions,  $D_C^{\text{alloy/silicate}}$  values determined in graphite-saturated systems have been used to predict C fractionation between cores

and MOs. This involves a key assumption that  $D_C^{\text{alloy/silicate}}$  was not dependent on bulk C content of the system. However, if partitioning of C between alloy and silicate melt follows non-Henrian behavior, i.e., activity coefficient of C in either alloy or silicate melt does not remain constant with increasing bulk C content, then the applicability of graphite-saturated  $D_C^{\text{alloy/silicate}}$  values to realistic, C-poor MOs would be compromised. A couple of recent studies (Kuwahara et al., 2021, 2019) using C-poor systems have shown that  $D_C^{\text{alloy/silicate}}$  values indeed depend upon bulk C content. However, the study of Kuwahara et al. (2019) had two critical limitations due to their usage of BN capsules – (1) the experiments produced silicate melt compositions with high  $B_2O_3$  contents (6.33–8.38 wt.%); and (2) the presence of wt.% levels of N in alloy and silicate phases which should have significantly diminished  $D_C^{\text{alloy/silicate}}$  values because N and C have strong negative and positive chemical interactions in the alloy and silicate melt phases, respectively (Grewal et al., 2021a, 2020, 2019b). Importantly, the experiments reported by Kuwahara et al. (2021, 2019) were in a limited  $fO_2$  range (IW–2.68 to IW–2.37). The amount of C dissolved in MOs, and consequently the amount of C available for partitioning into protoplanetary and planetary cores, is dependent on C speciation which is strongly affected by the  $fO_2$  of MOs during alloy-silicate equilibration. Therefore, to constrain C fractionation between cores and MOs for a wide range of rocky bodies in the inner Solar System, it is imperative to constrain  $D_C^{\text{alloy/silicate}}$  for C-poor systems at varying  $fO_2$ . See Table 1.

Here we present high  $P$ - $T$  experiments at 3 GPa–1700 °C using MgO capsules with varying amounts of bulk C to determine  $D_C^{\text{alloy/silicate}}$  in graphite-undersaturated conditions over a wide  $fO_2$  range (IW–6.35 to IW–2.59). We compare our  $D_C^{\text{alloy/silicate}}$  values with previous data and discuss the control of bulk C in addition to other thermodynamic parameters. Applying our new data to metal-silicate differentiation of inner Solar System bodies, we discuss the extent of C fractionation during their core formation.

## 2. Methods

### 2.1. Starting materials

A synthetic tholeiite basalt (ThB1) used in three previous alloy-silicate partitioning experimental studies (Grewal et al., 2021a, 2019b,a) was used as the starting silicate mixture (Supplementary Table 1; details in Supplementary Section). The alloy mixture was prepared using reagent grade Fe, Ni, and Si metals with or without vitreous carbon to create C-free to C-bearing starting mixtures (0C = 0 wt.% C, 1C = 1 wt.% C, 2C = 2 wt.% C; wt.% represents the mass percentage of C in the alloy mixture; Supplementary Table 1). Alloy and silicate mixtures were mixed in a mass ratio of 3:7. The experimental products yielded large glassy pools in MgO capsules at extremely reducing conditions because the addition of MgO from the capsule wall and the resulting depolymerization of the melt was counterbalanced by an increase in silicate melt polymerization due to the reaction:



Given our goal was to obtain glassy silicate melt domains, we started with extremely reduced conditions, i.e., a high proportion of metallic Si in the alloy mix. We then gradually modified the starting compositions (by lowering Si content) to achieve higher  $f_{\text{O}_2}$ s (Table 1) until we obtained large enough glassy melt pools necessary for reliable ion probe measurements.

### 2.2. High pressure-temperature experiments

The experiments were performed at 3 GPa–1700 °C in crushable MgO capsules (Table 1). An end-loaded piston cylinder device at Rice University with a 1/2-inch BaCO<sub>3</sub>/crushable MgO assembly and straight-walled graphite heaters was used to perform the experiments following the calibration and procedure of Tsuno and Dasgupta (2011). A Type C thermocouple was used to monitor and control the temperature. To minimize leakage of alloy melts, each experiment was sintered overnight at ~850 °C to reduce the porosity of capsules (Grewal et al., 2021a, 2019b,a) followed by heating to target temperature. After de-pressurization, the recovered samples were cut longitudinally using a W-wire saw. The samples were mounted in Crystalbond™, ground with a 1200-grit SiC, and polished down to 0.3 µm using a velvet cloth and alumina slurry. After polishing, Crystalbond™ was removed from the samples by soaking them overnight in acetone.

### 2.3. Approach to equilibrium

We performed a time series at 1, 2, 6, and 12 h to determine the time required to attain steady state chemical compositions. The time series was performed with a nominally C-free starting mixture (70% Thb1+30% Fe-5Ni-0C-12.5Si), yet both alloy and silicate melt phases contained C (Supplementary Fig. 1A, B). C contents in the alloy and silicate melts for nominally C-free systems did not show any systematic variation with time; therefore, nominally C-free experiments were used to estimate  $D_{\text{C}}^{\text{alloy/silicate}}$  for the lowest bulk C. The potential source of C was likely atmospheric contamination during the preparation of the starting mixtures. Continuous diffusion of C from the graphite heater during the experiments can be ruled as the primary C source because it should have led to variable C contents in the alloy and silicate melts as a function of time. Also, there was no spatial variability of C content in alloy and silicate melt domains. This indicates that the experiments had likely attained equilibrium with respect to exchange of C between the alloy and silicate melt phase in less than 1 h. The time series

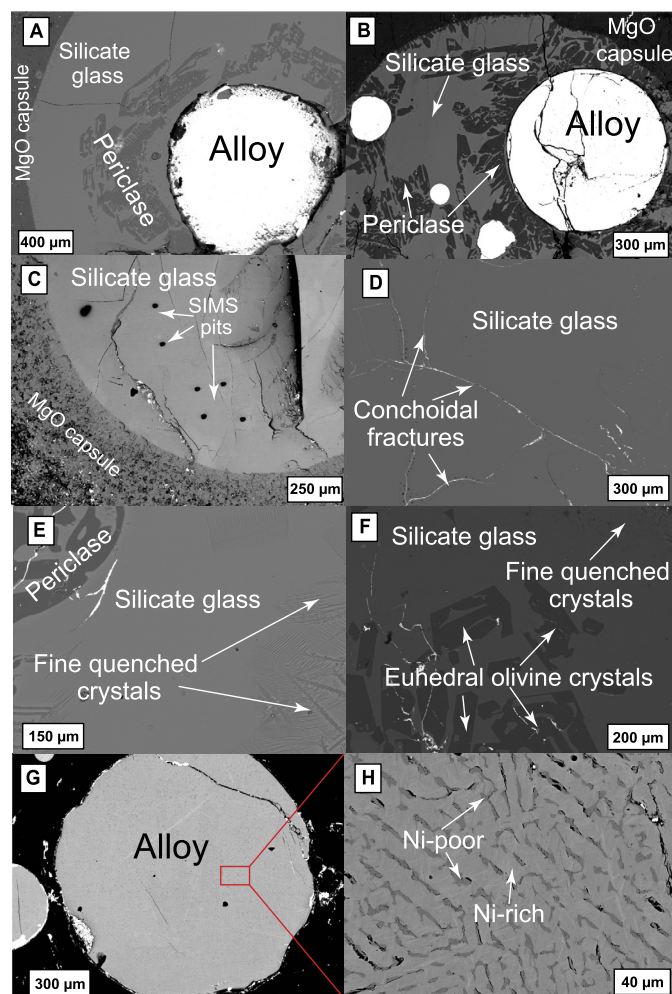


**Fig. 1.** Back-scattered electron (BSE) images of typical experimental products in crushable MgO capsules. (A, B) Co-existence of quenched alloy blobs and silicate glass with periclase (Exp. No. B481 and B482, respectively). (C) Location of SIMS pits in the silicate glass pools of experimental products (Exp. No. X72). (D) Silicate glass in Exp. No. B480 showing conchoidal fracture typical of amorphous materials. (E) Silicate melt comprising a glassy domain and a domain composed of mixtures of fine quenched crystals and glasses. Also shown in the upper left corner, equilibrium periclase (Exp. No. G640). (F) Silicate glass coexisting with euhedral olivine crystals (Exp. No. X85). (G, H) Detailed quenched texture of a metallic blob (Exp. No. G635).

experiments also showed that the reaction between the silicate starting mix and the MgO capsules reached steady state within 1 hr (Supplementary Fig. 1C, D). The rest of the experiments in this study, therefore, were performed for 1.5 h.

### 2.4. Analytical procedure

A JEOL JXA8530F Hyperprobe EPMA at the Department of Earth, Environmental, and Planetary Sciences, Rice University was used to measure major and minor element abundances in alloy and silicate melts as well as to measure C content in the alloy phase (Supplementary Table 2, 3). A Cameca IMS 1280 ion microprobe at Woods Hole Oceanographic Institution was used to determine bulk C and H contents in the silicate glasses. Analytical details are stated in the Supplementary Section.

## 3. Results

### 3.1. Texture of the experimental products

The experimental products quenched to spherical metal blobs embedded in a matrix of silicate glass and crystals (Fig. 1A, B). The

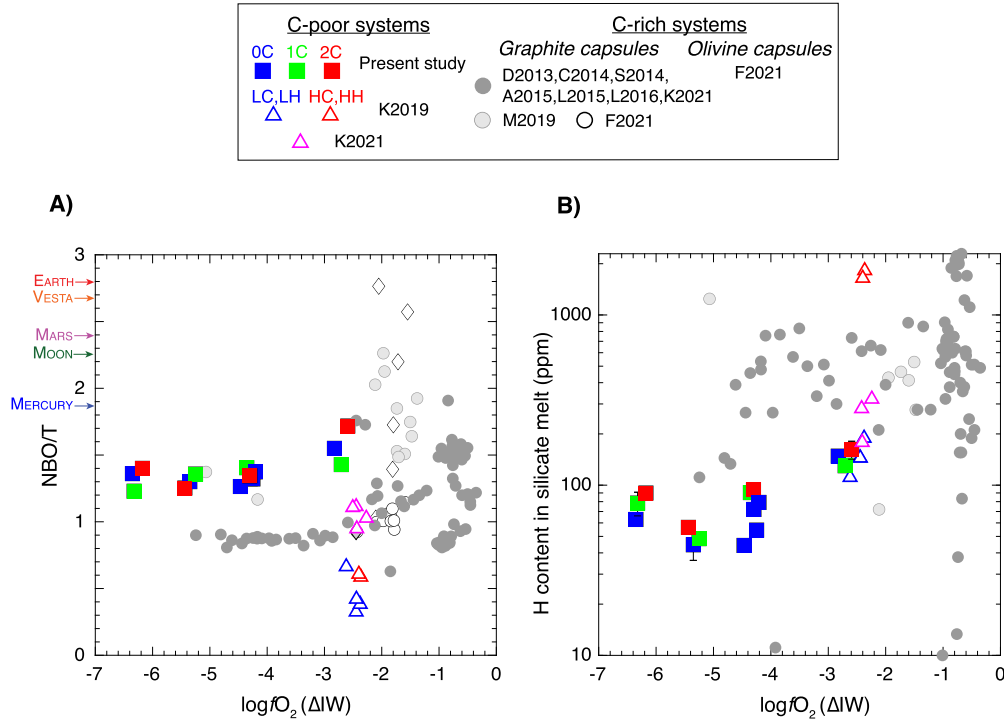


**Fig. 2.** A) Silicate melt compositions and B) bulk hydrogen contents in the experimental silicate melts as a function of oxygen fugacity. Across a wide  $fO_2$  range, the silicate melts of this study are more mafic and depolymerized (higher NBO/T) in comparison to those from previous experiments on  $D_C^{\text{alloy/silicate}}$  (except experiments of Fichtner et al. (2021) and Malavergne et al. (2019) between IW-2.2 and IW-1.6). Also, bulk H in the silicate melts of this study is lower than the majority of previous experiments on  $D_C^{\text{alloy/silicate}}$ . OC, 1C, and 2C represent the starting mixtures of this study with three different C contents in the alloy (Supplementary Table 1). LC, LH and HC, HH represent the low C, low H and high C, high H starting mixtures of Kuwahara et al. (2019) in BN capsules. Magenta triangles represent  $SiO_2$  capsule experiments of Kuwahara et al. (2021). Data in C-rich systems are compiled from previous studies that determined  $D_C^{\text{alloy/silicate}}$  in N- and S-free conditions for relatively shallow MOs at  $\leq 8$  GPa (A2015 = Armstrong et al. (2015); C2014 = Chi et al. (2014); D2013 = Dasgupta et al. (2013); F2021 = Fichtner et al. (2021); L2015 = Li et al. (2015); L2016 = Li et al. (2016); M2019 = Malavergne et al. (2019); S2014 = Stanley et al. (2014); K2021 = Kuwahara et al. (2021)). Thermodynamic parameter space for the data of previous studies:  $P = 1\text{--}12$  GPa,  $T = 1300\text{--}2300^\circ\text{C}$ ,  $\log fO_2 = IW-5.25$  to  $IW-0.35$ , NBO/T = 0.3–3.0, S content of alloy melt = 0–2 wt.%, and Si content of alloy melt = 0–10 wt.%. (A) KLB-1 peridotite composition is used to predict the MO composition of Earth (Davis et al., 2009). Primitive mantle compositions are used to estimate the MO compositions of Mars (Yoshizaki and McDonough, 2020), Mercury (Nittler et al., 2019), Moon (Taylor, 1982), and Vesta (Toplis et al., 2013).  $\pm 1 - \sigma$  standard deviations for NBO/T (based on replicate electron microprobe analyses) are smaller than the symbol sizes for all data from this study. Error bars for H content represent  $\pm 1 - \sigma$  standard deviation based on replicate ion probe analyses; where absent, the error bars are smaller than the symbol size. (For interpretation of the colors in the figure(s), the reader is referred to the web version of this article.)

volume of the glassy portion relative to the overall volume of the silicate melt decreased with increasing  $fO_2$ . Yet, even in the most oxidized experiments, the glassy portions were large enough that SIMS analyses could be performed (Fig. 1C, D, E). Ferropericlasite, produced as part of the experimental assemblage, was present adjacent to the metal blobs as well as dispersed in the silicate matrix (Fig. 1A, B, E). Euhedral olivine grains embedded in the silicate melt pool were present in two experiments (Fig. 1F). The alloy melt was composed of Ni-rich and Ni-poor quench phases (Fig. 1G, H). Graphite was not observed in any of the experimental products, indicating graphite-undersaturated conditions. None of the experiments showed any signs of vapor exsolution as rounded vesicles were absent in both metallic and silicate phases.

### 3.2. Silicate melt composition

NBO/T of the silicate melts varied between 1.2 and 1.7 (Fig. 2A). Although the silicate melts of this study have NBO/T values lower than peridotite-like MO compositions, they are more representative of MO differentiation in inner Solar System rocky bodies over a wide  $fO_2$  range as compared to many previous studies (except for the olivine and graphite capsule experiments of Fichtner et al. (2021) and Malavergne et al. (2019), respectively, between IW-2.2 and IW-1.6).

### 3.3. Hydrogen contents in the silicate melts

Hydrogen contents of the silicate melts lie within 44–161 ppm (Fig. 2B). These values are generally lower than those measured in silicate glasses from previous alloy-silicate experiments (except for a few experiments of Armstrong et al. (2015)). It is important to note that bulk H contents in the silicate glasses of Fichtner et al. (2021) were not reported.

### 3.4. Carbon contents in the silicate melts

Carbon contents in the silicate glasses are within the range of  $\sim 1\text{--}11$  ppm (Fig. 3A). These values are significantly lower than the C contents of graphite-saturated silicate melts, and are also lower than those of the silicate melts reported in the olivine capsule experiments of Fichtner et al. (2021) across the entire  $fO_2$  range but are similar to C-poor experiments of Kuwahara et al. (2021, 2019). In the experiments of this study and Kuwahara et al. (2019), C content in the silicate melt increases with increasing bulk C at a given  $fO_2$ . C contents show a V-shaped variation with  $\log fO_2$ , dropping with decreasing  $fO_2$  from IW-2.5 to IW-4.2 followed by an increase with a further decrease in  $fO_2$  (refer to Supplementary Section for  $fO_2$  calculation details). As reviewed by Dasgupta and Grewal (2019), a similar V-shaped variation of silicate melt C content with  $\log fO_2$  was also observed in graphite-saturated experiments, albeit with the inflection occurring at  $\sim IW-2$ .



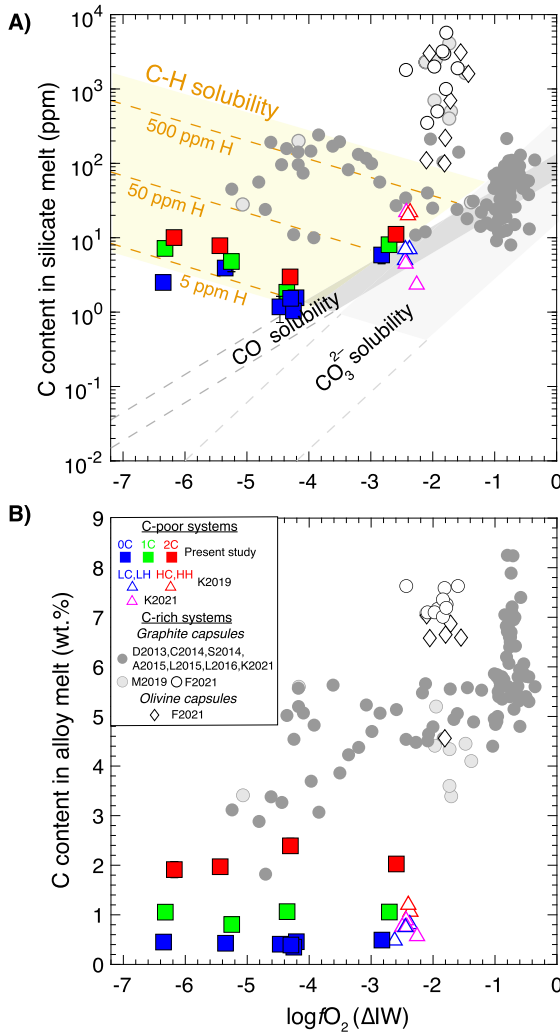


**Fig. 3.** Carbon content in **A)** silicate and **B)** Fe-rich alloy melts as a function of oxygen fugacity. C contents in the silicate and alloy melts of this study are systematically lower than those of previous studies (reference to the legend is the same as in Fig. 2). C contents in both silicate and alloy melts increase with increasing bulk C at a given  $fO_2$ . Also, C contents in the silicate melts of this study show a V-shaped trend with decreasing  $fO_2$  from  $\sim IW-2.5$  to  $\sim IW-4.2$  followed by an increase with further decrease in  $fO_2$ . Using thermodynamic models, the predicted C solubility as  $CO_3^{2-}$ , CO, and C-H is also plotted for comparison. C contents in graphite-undersaturated silicate melts of this study follow the  $CO_3^{2-} + CO$  solubility trend (grey colored bands and dashed lines) for  $\log fO_2 \geq IW-4.5$ , while graphite saturated silicate melts follow the same trend at  $\log fO_2 > IW-2$ . Lower bulk H contents in the silicate melts of this study make the C-H speciation important at more reduced conditions in comparison with graphite saturated melts containing higher bulk H. C contents in the silicate melts of Fichtner et al. (2021) and majority of the data of Malavergne et al. (2019) cannot be explained by the contribution of anhydrous  $CO_3^{2-} + CO$  or hydrous C-H species, or by bulk C solubility models based on previous experiments (e.g., Li et al. (2017) and Kuwahara et al. (2019); Supplementary Fig. 7)). The range of  $CO_3^{2-}$  solubility was calculated based on the experimental conditions of this study and previous studies using the C solubility model of Eguchi and Dasgupta (2018). CO solubility was calculated based on the models for MORB and rhyolite glass by Yoshioka et al. (2019). C-H solubility (yellow colored band) with different bulk H contents (orange dashed lines) was calculated at  $\log fO_2 < IW-1$  using the bulk C solubility model of Li et al. (2017). Error bars for C content in alloy and silicate melt from this study represent  $\pm 1 - \sigma$  standard deviation based on the replicate electron microprobe and SIMS analyses, respectively; where absent, the error bars are smaller than the symbol size.

### 3.5. Carbon contents in the alloy melts

Carbon contents in the alloy melts of this study are comparable with those of Kuwahara et al. (2021, 2019) but are distinctly lower than C contents of graphite-saturated alloys as well as alloys in the olivine capsule experiments of Fichtner et al. (2021)

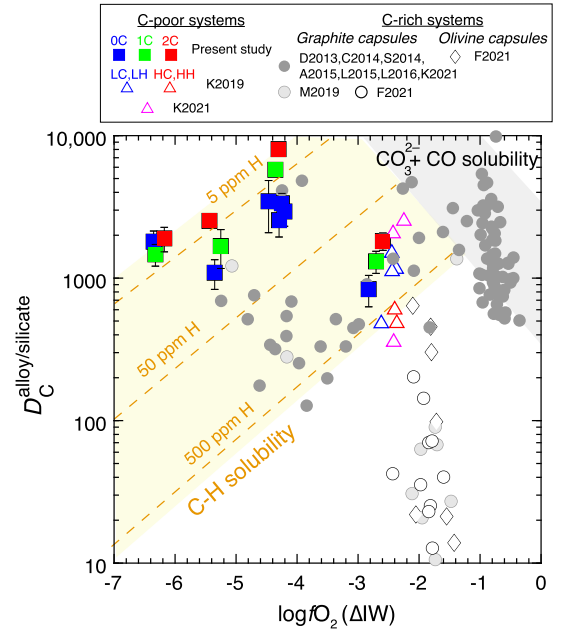


**Fig. 4.**  $D_C^{\text{alloy/silicate}}$  as a function of oxygen fugacity. In this study,  $D_C^{\text{alloy/silicate}}$  increases with increasing bulk C content at a given  $fO_2$  for graphite-undersaturated conditions.  $D_C^{\text{alloy/silicate}}$  values in this study roughly follow an inverse V-trend with decreasing  $fO_2$  from  $\sim IW-2.5$  to  $\sim IW-4.2$  followed by a decrease at  $\log fO_2 < \sim IW-4.2$ . Plotted for comparison are  $D_C^{\text{alloy/silicate}}$  from previous studies (both graphite-undersaturated as well as graphite-saturated and/or systems with C-rich alloys; the reference to the legend is same as in Fig. 2). The grey and yellow bands (with orange dashed lines) are the predictions of  $D_C^{\text{alloy/silicate}}$  values for scenarios where  $CO_3^{2-} + CO$  and C-H, respectively, are the dominant C species in silicate melts (following C solubility in silicate melts shown in Fig. 3A). These bands largely capture the systematics developed for graphite-saturated, and somewhat more hydrous, metal-silicate systems explored in the previous studies and highlight how such trends are offset from those obtained in this study for graphite-absent and H-poor conditions. Error bars for  $D_C^{\text{alloy/silicate}}$  from this study represent  $\pm 1 - \sigma$  standard deviation obtained by propagation of  $\pm 1 - \sigma$  standard deviation on C content in the alloy and silicate melts; where absent, the error bars are smaller than the symbol size.

(Fig. 3B). C contents in the alloy melts of 0C systems are broadly in agreement with the nominally C-free experiments of Grewal et al. (2021a). At a given  $fO_2$ , C contents in the alloys increase with increasing bulk C. Averaged C contents in alloys for 0C, 1C, and 2C systems are  $0.42 \pm 0.05$ ,  $0.99 \pm 0.13$ , and  $2.07 \pm 0.22$  wt.%, respectively (errors are  $1 - \sigma$  standard deviation). A similar increase in C content of alloys with increasing bulk C was also reported by Kuwahara et al. (2019). For a given bulk C content, C contents in the alloys do not vary with  $fO_2$ . This observation is in contrast with graphite-saturated alloys where C solubility in the alloys decrease with decreasing  $fO_2$  (at  $\log fO_2 < IW-2.5$ ) due to an increase in their Si contents (Supplementary Fig. 2; Grewal et al., 2019a; Li et al., 2016, 2015).

### 3.6. Partition coefficient of carbon between alloy and silicate melt

$D_C^{\text{alloy/silicate}}$  values in this study vary between 837 and 8045 (Fig. 4). At a given  $fO_2$ ,  $D_C^{\text{alloy/silicate}}$  increases with increasing bulk C.  $D_C^{\text{alloy/silicate}}$  values follow an inverted V-trend in  $fO_2$  space, increasing from  $\sim IW-2.5$  to  $\sim IW-4.2$  followed by a drop at more reducing conditions. This trend follows that of C contents in the silicate melts in an inverse manner. An inverted V-trend of  $D_C^{\text{alloy/silicate}}$  in  $fO_2$  space was also observed in graphite-saturated conditions with the inflection occurring at  $\sim IW-2$  (Li et al., 2016, 2015).  $D_C^{\text{alloy/silicate}}$  values determined in C-poor experiments of Kuwahara et al. (2021, 2019) are comparable with those measured in

this study. Interestingly, the experiments of Kuwahara et al. (2019) with higher bulk C contents have lower  $D_C^{\text{alloy/silicate}}$ . As the higher bulk C experiments of Kuwahara et al. (2019) also had an order of magnitude higher bulk H (Fig. 3B), we suggest that their lower  $D_C^{\text{alloy/silicate}}$  values at higher bulk C are related to an increase in C solubility in the silicate melts at higher bulk H (discussed in Section 4.1). Between IW-2.2 and IW-1.6,  $D_C^{\text{alloy/silicate}}$  values from Fichtner et al. (2021) and Malavergne et al. (2019) are significantly lower than those determined in this study and all previous studies in a similar  $P$ - $T$  range.

#### 4. Discussion

The effects of relevant thermodynamic parameters on  $D_C^{\text{alloy/silicate}}$  can only be ascertained by determining their individual effects on C contents in the alloy and silicate melts. Bulk C content of the system and  $fO_2$  are the primary parameters investigated in this study for relatively H-poor, mafic-ultramafic silicate melts. As shown in the previous section, the interplay of these two parameters directly controls the relative distribution of C in alloy and silicate melts.

##### 4.1. Effect of oxygen fugacity, bulk hydrogen, and silicate melt composition on $D_C^{\text{alloy/silicate}}$

$D_C^{\text{alloy/silicate}}$  values in both graphite-undersaturated and graphite-saturated conditions display inverted-V trends as a function of  $fO_2$ , but these trends are offset in  $fO_2$  space (Fig. 4). The offset of these trends in  $fO_2$  space can be reconciled with the expected C speciation in the silicate melts.

C can potentially dissolve as  $CO_3^{2-}$  complexes, molecular CO, or hydrated C-H species in reduced, mafic-ultramafic silicate melts relevant for core-mantle differentiation (e.g., Dasgupta and Grewal, 2019; Keppler and Golabek, 2019). The speciation of C-O-H volatiles in reduced silicate melts has been determined by Raman and FTIR spectroscopy in previous studies (e.g., Dalou et al., 2019; Grewal et al., 2020 and references therein). Raman spectroscopy is used to ascertain the presence of C-H (Armstrong et al., 2015; Chi et al., 2014; Dalou et al., 2019; Grewal et al., 2020; Li et al., 2015) and C=O in silicate melts (Wetzel et al., 2013; Yoshioka et al., 2015), while FTIR is used to determine the presence of  $CO_3^{2-}$  (Armstrong et al., 2015; Duncan et al., 2017). Similar to the observations of Grewal et al. (2020), high fluorescence levels in glassy pools generated at  $\log fO_2 < IW-2.5$  rendered Raman spectroscopy ineffective to determine the presence of C-H and C=O species in the silicate glasses of this study. On the other hand, extremely low concentrations of C and H led to inconclusive FTIR spectra. Therefore, to determine the relative contribution of these three species, we used graphite-saturated  $CO_3^{2-}$  (Eguchi and Dasgupta, 2018), CO (Yoshioka et al., 2019), and bulk C (accounting for C-H as well) (Li et al., 2017) solubility models (Fig. 3A).  $CO_3^{2-}$  solubility range was calculated within the  $P$  (1–12 GPa)- $T$  (1300–2300 °C)- $fO_2$  (IW-6.35 to IW-0.35)-NBO/T (0.3–3.0) range of this study and all previous studies. It is important to note that although the  $CO_3^{2-}$  solubility model of Eguchi and Dasgupta (2018) was not calibrated at  $\log fO_2 < IW-2$ , its predictions in the more reduced range are robust as they derive from the dependence of  $fCO_2$  on  $fO_2$  in graphite oxidation reaction. The predictions of that study are also in broad agreement with the thermodynamic calculations of Keppler and Golabek (2019). CO solubility is not known for silicate melt compositions relevant for this study (NBO/T = 1.23–1.72). Hence, CO solubility was calculated based on the CO solubility models for both MORB and rhyolite glasses by Yoshioka et al. (2019). Total C dissolved as  $CO_3^{2-} + CO$  decreases with decreasing  $fO_2$  with  $CO_3^{2-}$  dissolution being dominant at  $\log fO_2$

$> IW-2$  and CO dissolution dominating at more reducing conditions (Fig. 3A). C content in the silicate melts of this study and C-poor experiments of Kuwahara et al. (2021, 2019) fall along the C solubility trend of  $CO_3^{2-} + CO$  down to IW-4.5. This may indicate that the silicate melts of this study are close to their C saturation limits. However, it must be noted that the thermodynamic models – especially for CO solubility, which dominates in the  $fO_2$  range relevant for our experiments – were not calibrated for the depolymerized silicate melt compositions of this study. Also, a systematic increase of C content in the silicate melts of this study with increasing bulk C at any given  $fO_2$  indicates that the silicate melts did not reach C saturation limits (Fig. 3A). C-H species become important only at  $\log fO_2 < IW-4.5$  because adequately high  $fH_2$  (or the amount of H available to bond with C rather than O) is imposed only at extremely low  $fO_2$ s (tracked by the reaction:  $H_2O_{(g)} = H_{2(g)} + 1/2 O_{2(g)}$ ) due to low bulk H contents in the silicate melts of this study. This is in contrast to the graphite saturated silicate melts of previous studies which contain higher bulk H contents. As a result, C solubility as  $CO_3^{2-} + CO$  can only explain C contents in graphite saturated silicate melts at  $\log fO_2 > IW-2$ , below which C-H species is dominant due to higher bulk H. These considerations may explain why the trend reversal for C contents in the silicate melts (Fig. 3A) and  $D_C^{\text{alloy/silicate}}$  (Fig. 4) takes place at more reduced conditions in this study. A combination of lower bulk H contents and an increase in the solubility of both  $CO_3^{2-}$  and CO with greater depolymerization of the silicate melts (Duncan et al., 2017; Yoshioka et al., 2019) might explain the dominance of  $CO_3^{2-} + CO$  species in the silicate melts of this study over a wider  $fO_2$  range.  $D_C^{\text{alloy/silicate}}$  in graphite undersaturated silicate melts of Kuwahara et al. (2019) and Kuwahara et al. (2021) with lower (0.32–0.66) and higher (0.95–1.11) NBO/T values, respectively, are broadly similar with the  $D_C^{\text{alloy/silicate}}$  values of the most oxidized experiments of this study with more depolymerized silicate melts (NBO/T = 1.43–1.72) (Fig. 2A, 4). This suggests that the effect of silicate melt compositions on  $D_C^{\text{alloy/silicate}}$  may not be critical in C-poor conditions. This observation is in contrast to the conclusions of Fichtner et al. (2021) predicting a dominating effect of NBO/T on C dissolution in silicate melts.

C contents in the silicate melts of graphite capsule (350–5700 ppm) and olivine capsule experiments (100–3100 ppm) from Fichtner et al. (2021) are completely offset from the data of this study and all previous studies performed under similar conditions (Fig. 3A). C contents in the silicate melts of Fichtner et al. (2021) cannot be explained by the contribution of anhydrous  $CO_3^{2-} + CO$  and/or hydrated C-H species even at graphite saturation (e.g., Eguchi and Dasgupta, 2018; Li et al., 2017; Yoshioka et al., 2019) and likely represent products that are in redox disequilibrium with the coexisting metals (discussed in detail in Supplementary Section). Similarly, C content in the silicate melts of Malavergne et al. (2019) (NBO/T = 1.17 to 2.26) are offset from all previous data at  $\sim IW-2$ . Anomalously high C contents in their silicate melts may be caused by their inability to quench their silicate melts to glasses (except for one experiment (Sample No. O2-16)). Chi et al. (2014) demonstrated that silicate melts without homogeneous glassy pools always yielded 2–10 times higher C concentrations in comparison to glassy pools under similar  $P$ - $T$ - $fO_2$ . It is important to note that the most depolymerized, graphite saturated silicate melts of Kuwahara et al. (2021) (NBO/T  $\sim 1.75$ ) have C contents that are broadly within the range of previous studies in graphite saturated systems (except for Malavergne et al. (2019)). Because Malavergne et al. (2019) reported anomalously high C contents in their silicate melts for experiments done in a  $P$ - $T$ - $fO_2$  range similar to previous studies in graphite saturated conditions, we suspect the majority of their reported silicate melt C contents are unlikely to be reliable. As a result, extremely low  $D_C^{\text{alloy/silicate}}$  val-

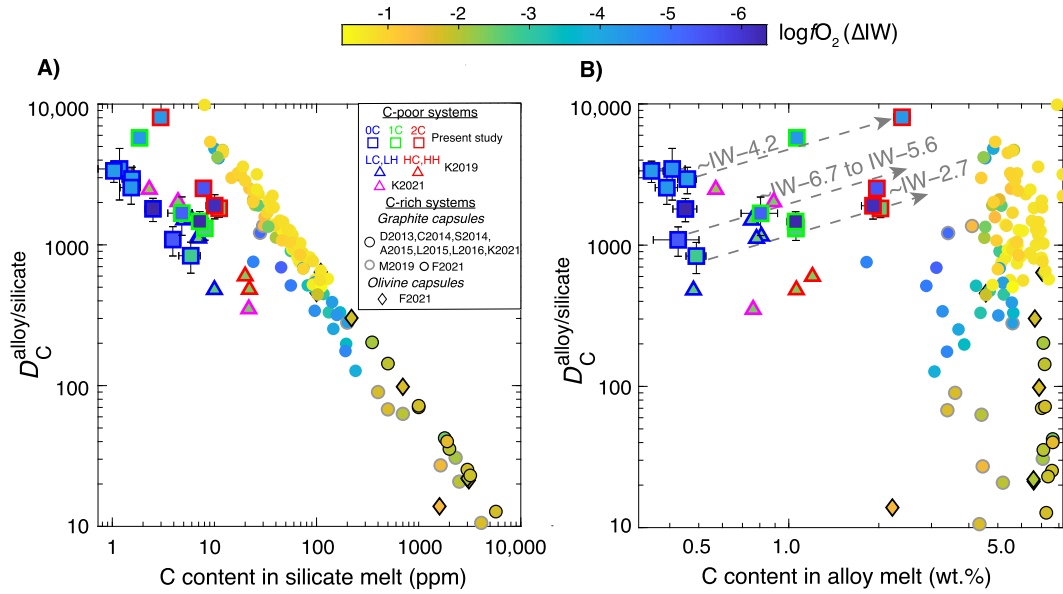


**Fig. 5.** Variation of  $D_C^{\text{alloy/silicate}}$  with C contents in **A)** silicate and **B)** alloy melts as a function of oxygen fugacity. For C-rich systems,  $D_C^{\text{alloy/silicate}}$  scales only with C content in the silicate melt (panel A). However, in C-poor, graphite-absent systems,  $D_C^{\text{alloy/silicate}}$  scales both with C content in the silicate (**A**) and alloy melt (**B**) at a given  $fO_2$ . Lines in panel **B**) depict the trend of  $D_C^{\text{alloy/silicate}}$  variation with increase in C content of the alloy melt within a given  $fO_2$  range. Error bars for the data from the present study represent  $\pm 1 - \sigma$  standard deviation obtained by propagation of  $\pm 1 - \sigma$  standard deviation on C content in the alloy and silicate melts; where absent, the error bars are smaller than the symbol size. The reference to previous studies in the legend is the same as in Fig. 2.

ues reported by Fichtner et al. (2021) and Malavergne et al. (2019) between IW-2.2 and IW-1.6 (Fig. 4), may not represent true equilibrium values.

#### 4.2. Effect of bulk carbon content on $D_C^{\text{alloy/silicate}}$

In this study, C contents in both alloy and silicate melts increase with increasing bulk C at a given  $fO_2$  (Fig. 3A, B). Importantly, increase in bulk C also leads to an increase in  $D_C^{\text{alloy/silicate}}$  (Fig. 4). Previous data for C-rich alloys, i.e., experiments conducted in graphite-saturated conditions as well as the olivine capsule experiments of Fichtner et al. (2021), show that the variation of  $D_C^{\text{alloy/silicate}}$  is sensitive to C contents in the silicate melts only (Fig. 5A). This is because C contents in the silicate melts vary between 2-3 orders of magnitude with change in  $fO_2$  and the variation in C contents of the alloys is minimal (except for extremely reduced experiments where C solubility in Si-bearing alloys is an order of magnitude lower relative to Si-free alloys; Fig. 5A, B). As a result, variation of  $D_C^{\text{alloy/silicate}}$  values in C-rich alloy melt-bearing systems is mainly controlled by C concentration in the silicate melts (which is directly dependent on  $fO_2$ , bulk H content, and silicate melt composition). Whereas the data from graphite-undersaturated experiments of this study show that at a given  $fO_2$ ,  $D_C^{\text{alloy/silicate}}$  values are sensitive to the variation in both C contents in silicate (Fig. 5A) and alloy melts (Fig. 5B).

What causes  $D_C^{\text{alloy/silicate}}$  to vary with bulk C? Partition coefficient of a component follows Nernst's distribution law if its dissolution demonstrates Henrian behavior in both phases, i.e., its activity is directly proportional to its concentration (Beattie, 1993). In other words, the activity coefficient of a component in a given phase must not change with its concentration. Under this condition, partition coefficients are independent of the concentration of the component and depend only on other intensive and extensive variables (e.g.,  $P$ ,  $T$ ,  $fO_2$  and composition of alloy and silicate melts in the case of  $D_C^{\text{alloy/silicate}}$ ). Fig. 6A shows that activity coefficients of carbon in the alloy melts ( $\gamma_C^{\text{alloy melt}}$ ) for graphite-saturated alloys are within the range of 4-6.5 (higher

values at more reducing conditions are a result of non-ideal interactions between Si and C;  $\gamma_C^{\text{alloy melt}}$  values are reported using graphite as the standard state; see Supplementary Section for details).  $\gamma_C^{\text{alloy melt}}$  increases with decreasing  $fO_2$  in graphite-undersaturated alloys as well due to similar non-ideal interactions between Si and C. Importantly, at a given  $fO_2$ ,  $\gamma_C^{\text{alloy melt}}$  increases with increasing C content in alloys until the alloys reach their C saturation limit (Fig. 6B). This is because substitutional sites in the alloy melts having lowest chemical potential are readily available for C substitution at low C concentrations whereas at large C concentrations the number of sites is insufficient to incorporate more C atoms. This causes C atoms to exert mutual repulsions on each other at higher concentrations. These non-ideal interactions are exacerbated for graphite-saturated alloys due to an extremely large concentration of C atoms vying for similar substitutional sites in the alloy melt. The observed increase of  $\gamma_C^{\text{alloy melt}}$  with increasing C content in the alloy is in agreement with the predictions of metallurgy literature at 1 bar for Fe-metallic melts (e.g., Bouchard and Bale, 1995; Wang et al., 1991).

An increase of  $\gamma_C^{\text{alloy melt}}$  with increasing bulk C content confirms that C dissolution in alloy melts does not follow Henry's law with variations in bulk C content of the system. Therefore, it is critical to incorporate the effect of bulk C on  $D_C^{\text{alloy/silicate}}$  in addition to other thermodynamic variables to predict its core-mantle partitioning behavior in MOs. More importantly, this demonstrates that  $D_C^{\text{alloy/silicate}}$  determined for C-poor alloys allow for more accurate predictions on equilibrium C fractionation between MOs and cores of the rocky bodies, which likely occurred in C-poor conditions.

#### 4.3. Effect of pressure and temperature on $D_C^{\text{alloy/silicate}}$

Because the experiments in this study were conducted at a fixed  $P$ - $T$ , the effect of  $P$  and  $T$  on  $D_C^{\text{alloy/silicate}}$  cannot be directly established from our experiments. However, it is important to note that even though the experiments of Kuwahara et al. (2019) were conducted in a higher  $P$ - $T$  range (4-12 GPa and 1700-2000 °C) than this study (3 GPa and 1700 °C) and Kuwahara

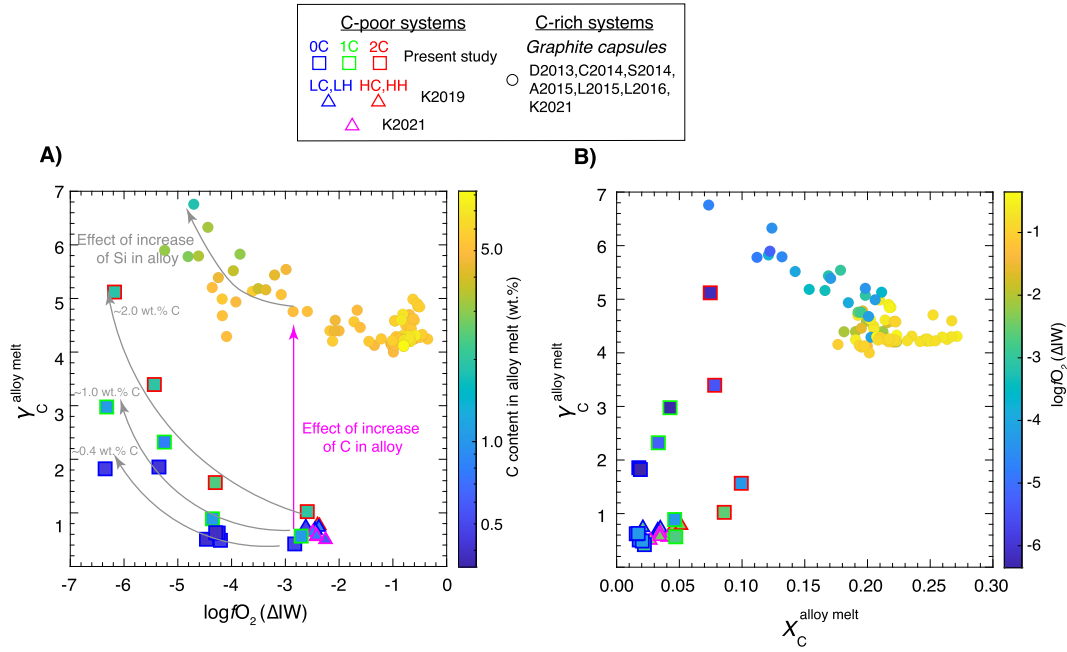


**Fig. 6.** Activity coefficient of carbon in alloy melt ( $\gamma_C^{\text{alloy melt}}$ ), with graphite as the standard state, as a function of – (A) oxygen fugacity and (B) mole fraction of C in the alloy melt ( $X_C^{\text{alloy melt}}$ ). At a given  $fO_2$ ,  $\gamma_C^{\text{alloy melt}}$  increases with increasing C content in the alloy melt such that graphite saturated alloy melts have significantly higher  $\gamma_C^{\text{alloy melt}}$  values relative to graphite-undersaturated alloys. The increase in  $\gamma_C^{\text{alloy melt}}$  with increasing C content of the alloy is due to mutual repulsions amongst C atoms vying for limited substitutional sites in the alloy melt. Also,  $\gamma_C^{\text{alloy melt}}$  increases with decreasing  $fO_2$  due to non-ideal interactions between C and Si atoms. Three hand-drawn curves with arrows in (A) mark the observed dependence of  $\gamma_C^{\text{alloy melt}}$  with  $\log fO_2$  and alloy melt C contents (with the alloy melt C contents marked against each curve).

et al. (2021) (2 GPa and 1650 °C),  $D_C^{\text{alloy/silicate}}$  values of these studies are comparable at  $\sim IW-2.8$ . This suggests that the effect of  $P-T$  on  $D_C^{\text{alloy/silicate}}$  in graphite-undersaturated conditions is not pronounced up to 12 GPa. This is in stark contrast to the results of Fischer et al. (2020) at 37–59 GPa and 3927–4927 °C, where the authors, using a diamond anvil setup, reported extremely low  $D_C^{\text{alloy/silicate}}$  values ( $\sim 1-35$ ) ascribed to anomalously high C content in their silicate melts. However, the reported C contents in their silicate melts using SIMS and EPMA had almost an order of magnitude difference and the cause of this difference was largely unexplained. The experimental products of that study showed a widespread dispersal of nanoscale metallic blebs through the silicate melt, which can significantly affect their measured C concentration in their silicate melts owing to the highly siderophile character of C. It remains unclear whether such metallic globules were equilibrium phases or were exsolved from the silicate melts during quench. Blanchard et al. (2019) reported  $D_C^{\text{alloy/silicate}}$  between 23 and 157 at 56–71 GPa and 3327–3727 °C using diamond anvil cell experiments in a similar  $fO_2$  range as Fischer et al. (2020). C concentrations in their silicate melts were at least an order of magnitude lower than those measured by Fischer et al. (2020). Importantly, Blanchard et al. (2019) avoided metallic blebs while measuring C contents in their silicate melt phases. Therefore, it is reasonable to argue that the measurements of C contents in the silicate phase, and consequently  $D_C^{\text{alloy/silicate}}$  values, were compromised in the study of Fischer et al. (2020) because of the inclusion of metallic globules in the silicate phase measurements along with the analysis of a heterogeneous aggregate. In agreement with the data of Blanchard et al. (2019), we conclude that although  $D_C^{\text{alloy/silicate}}$  was lower in deeper MOs, the effect of high  $P-T$  is might not be as pronounced as claimed by Fischer et al. (2020).

#### 4.4. Prediction of $D_C^{\text{alloy/silicate}}$ values applicable for rocky bodies in the inner Solar System having C-poor cores

Previous studies in graphite-saturated conditions show that C acts as a moderately to highly siderophile element during core-mantle differentiation in shallow MOs (e.g., Armstrong et al., 2015; Chi et al., 2014; Dasgupta et al., 2013; Stanley et al., 2014). This should have led to almost all of the accreted C to be sequestered in protoplanetary and planetary cores, resulting in severe depletion of C in their bulk silicate reservoirs. However, as outlined in the introduction, several lines of evidence suggest that formation of C-rich alloys may not have been the norm during differentiation of planetesimals, planetary embryos, and Earth-like planets. The parent cores of magmatic iron meteorites – including those whose parent bodies accreted C-rich carbonaceous chondrite-like materials – contained only 0.02–0.11 wt.% C (Hirschmann et al., 2021). Geochemical estimates place upper bounds on the C content of Earth's core between  $\sim 0.4$  wt.% (Dasgupta and Grewal, 2019) and  $\sim 1$  wt.% (Wood et al., 2013). A C-poor nature of Earth's core has also been predicted by numerical models accounting for the complexity of Earth's growth (Blanchard et al., 2019; Fischer et al., 2020). Mineral physics constraints on the effect of C and other light elements on the physical properties of liquid iron alloy also suggest that C is not likely to be a major light element in Earth's core (e.g., Badro et al., 2014). Similarly low C contents in Martian core have been predicted by geochemical and geophysical models (Brennan et al., 2020; Tsuno et al., 2018). These lines of evidence suggest that the  $D_C^{\text{alloy/silicate}}$  values determined using C-rich alloys may not be applicable for C-poor MOs that were prevalent in the rocky bodies of the Solar System.

Given we determined the variation of  $D_C^{\text{alloy/silicate}}$  using relatively C-poor alloys (containing  $\sim 0.4$ , 1, and 2 wt.% C), our data better capture alloy-silicate fractionation of C in inner Solar System rocky bodies. Bulk H content in the silicate melts of this study (44–161 ppm) lies well within the range of bulk H measured in



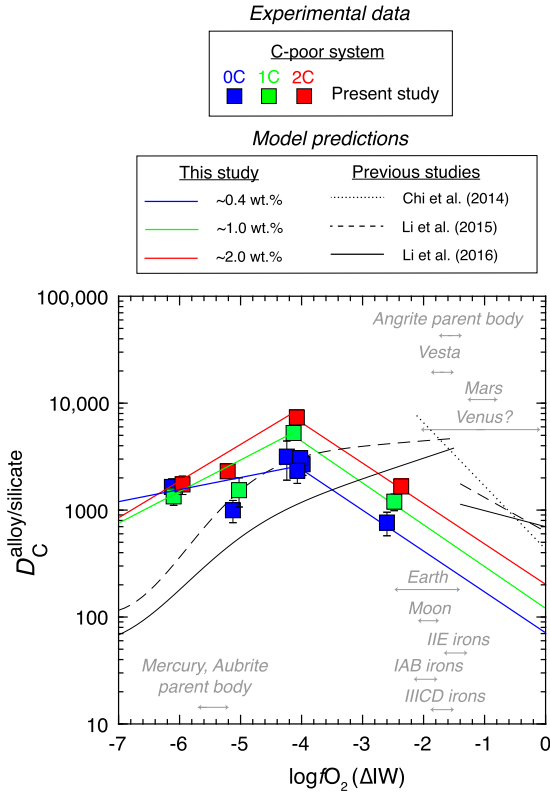


**Fig. 7.** Predicted  $D_{\text{C}}^{\text{alloy/silicate}}$  values as a function of  $f_{\text{O}_2}$  using graphite-undersaturated experimental data from this study. Solid color lines represent a linear fit of the  $D_{\text{C}}^{\text{alloy/silicate}}$  data from this study as a function of  $f_{\text{O}_2}$  for a fixed C content in the alloy (blue = ~0.4 wt.% C, green = ~1 wt.% C, and red = ~2 wt.% C).  $D_{\text{C}}^{\text{alloy/silicate}}$  values predicted by parameterized equations from the previous studies for shallow, graphite saturated MOs are also shown for comparison. Average experimental condition of this study ( $P = 3$  GPa,  $T = 1700$  °C,  $\text{NBO/T} = 1.4$ , and bulk H content of the silicate melt = 80 ppm) is used to calculate the predicted  $D_{\text{C}}^{\text{alloy/silicate}}$  values from the previous studies.  $f_{\text{O}_2}$  of average core-mantle differentiation conditions for rocky bodies in the inner Solar System are compiled from Righter et al. (2016).

enstatite chondrites and aubrites (86–596 ppm; Piani et al., 2020). As most of the material accreted by inner Solar System protoplanets and planets was isotopically similar to enstatite chondrites and aubrites (Dauphas, 2017), bulk H content of the silicate melts of this study replicate the degree of hydration of inner Solar System MOs. Therefore, an extrapolation of  $D_{\text{C}}^{\text{alloy/silicate}}$  values of this study in the  $f_{\text{O}_2}$  space can be used to predict  $D_{\text{C}}^{\text{alloy/silicate}}$  relevant for alloy-silicate equilibration in a wide range of rocky bodies (Fig. 7). In Fig. 7, the solid color lines represent linear fits of the  $D_{\text{C}}^{\text{alloy/silicate}}$  data from this study as a function of  $f_{\text{O}_2}$  for a fixed C content in the alloy (blue = ~0.4 wt.% C, green = ~1 wt.% C, and red = ~2 wt.% C). At  $>IW-4.2$ ,  $\ln D_{\text{C}}^{\text{alloy/silicate}} = -0.88 \times \log f_{\text{O}_2} (\Delta IW) + 4.26$ ,  $= -0.90 \times \log f_{\text{O}_2} (\Delta IW) + 4.76$ ,  $= -0.87 \times \log f_{\text{O}_2} (\Delta IW) + 5.25$  for ~0.4, ~1, and ~2 wt.% C in the alloy, respectively. At  $<IW-4.2$ ,  $\ln D_{\text{C}}^{\text{alloy/silicate}} = 0.26 \times \log f_{\text{O}_2} (\Delta IW) + 8.91$ ,  $= 0.68 \times \log f_{\text{O}_2} (\Delta IW) + 11.38$ ,  $= 0.79 \times \log f_{\text{O}_2} (\Delta IW) + 12.32$  for ~0.4, ~1, and ~2 wt.% C in the alloy, respectively. These predictions are also compared with the projected  $D_{\text{C}}^{\text{alloy/silicate}}$  values from previous studies in a  $P$ - $T$ - $\text{NBO/T}$ - $X$  range similar to this study ( $P = 3$  GPa,  $T = 1700$  °C,  $\text{NBO/T} = 1.4$ , bulk H content of the silicate melt = 80 ppm, and Ni and S content of alloy = 5 and 0 wt. %, respectively; Chi et al., 2014; Li et al., 2016, 2015). It is important to note that these are first order predictions only because the effects of  $P$ ,  $T$ , and  $\text{NBO/T}$  on  $D_{\text{C}}^{\text{alloy/silicate}}$  are largely unknown in C-poor conditions. Especially, if  $P$ - $T$  have a significant

effect on  $D_{\text{C}}^{\text{alloy/silicate}}$  in C-poor systems similar to those predicted by Blanchard et al. (2019) and Fischer et al. (2020) for C-rich systems, then the applicability of these parameterized equations for deep MO-like conditions could be limited. Future work is required to determine the effect of all relevant thermodynamic parameters to build a comprehensive  $D_{\text{C}}^{\text{alloy/silicate}}$  parameterization for C-poor MO systems.

As protoplanetary and planetary cores were likely C-poor, we used the  $D_{\text{C}}^{\text{alloy/silicate}}$  values determined for the most C-poor systems (blue lines in Fig. 7) to predict the  $D_{\text{C}}^{\text{alloy/silicate}}$  values applicable during core-mantle differentiation in rocky bodies. Based on C abundances in iron meteorites, our experimental data predict that  $D_{\text{C}}^{\text{alloy/silicate}}$  values between ~200 and 500 are applicable for core-mantle differentiation in the parent bodies of IAB, IIE and IIIAB irons. For Vesta and angrite parent body,  $D_{\text{C}}^{\text{alloy/silicate}} \sim 300$  is applicable during their core-mantle differentiation. For alloy-silicate equilibration in Moon,  $D_{\text{C}}^{\text{alloy/silicate}} \sim 400$  is applicable. For Mercury and aubrite parent body,  $D_{\text{C}}^{\text{alloy/silicate}} \sim 1800$ . Core-mantle differentiation in Mars is predicted to occur at higher  $P$  (13 GPa; Rai and Van Westrenen (2013)) relative to the experiments of this study (3 GPa). However, we noted that the predicted  $D_{\text{C}}^{\text{alloy/silicate}}$  values from our experiments are in agreement with those measured by Kuwahara et al. (2019) up to 12 GPa. Therefore, we use our experimental results to predict  $D_{\text{C}}^{\text{alloy/silicate}}$  of ~200 for core-mantle differentiation of Mars. It is important to note that the Martian core is predicted to be S-rich (10–19 wt.% S; Brennan et al., 2020; Rai and Van Westrenen, 2013) whereas the experimental alloys of this study are S-free. If C-S negative interactions similar to graphite saturated alloys (Grewal et al., 2019b; Tsuno et al., 2018) are also important for C-poor, S-rich alloys, then the  $D_{\text{C}}^{\text{alloy/silicate}}$  values applicable for Martian core-mantle differentiation could be lower than those predicted by this study. The predictive capacity of our experimental results maybe limited for deep MO events during Earth's core-mantle differentiation if  $P$ - $T$  have a significant effect on  $D_{\text{C}}^{\text{alloy/silicate}}$ . However, if there was a limited effect of  $P$ - $T$  on  $D_{\text{C}}^{\text{alloy/silicate}}$  beyond 12 GPa and 2000 °C, then our experimental results predict  $D_{\text{C}}^{\text{alloy/silicate}}$  of ~400 for an averaged single stage core formation (at ~IW-2) on Earth. This is in contrast to the extremely low  $D_{\text{C}}^{\text{alloy/silicate}}$  values (~0.5–1.8) predicted by Fischer et al. (2020) but are on a similar order of magnitude to the  $D_{\text{C}}^{\text{alloy/silicate}}$  values predicted by Blanchard et al. (2019). It should be noted that both studies, which aimed to measure  $D_{\text{C}}^{\text{alloy/silicate}}$  values in deep terrestrial MO-like conditions (Blanchard et al., 2019; Fischer et al., 2020), produced C-rich alloys. As the final stages of core formation in deep terrestrial MOs likely took place in C-poor conditions, it is critical to determine whether the effect of  $P$ - $T$  on  $D_{\text{C}}^{\text{alloy/silicate}}$  holds true for C-poor systems as well.

#### 4.5. Fractionation of C between metallic and silicate reservoirs in the present-day rocky bodies of inner Solar System

Using the newly derived  $D_{\text{C}}^{\text{alloy/silicate}}$  values from this study applicable for C-poor systems, we make first order predictions to constrain the fractionation of C between MO and cores in inner Solar System rocky bodies. Because the  $D_{\text{C}}^{\text{alloy/silicate}}$  values in this study were determined for  $P$ - $T$  conditions applicable during core-mantle differentiation in planetesimal and planetary embryo-sized bodies, we apply our results to Vesta, angrite parent body, Moon, Mars, and Mercury (Fig. 8). C abundances in the MOs and cores of these bodies were calculated via single stage core formation models which capture their average core-mantle differentiation conditions. C abundances in the MOs predicted by this study are significantly higher (in some cases by more than an order of magnitude)

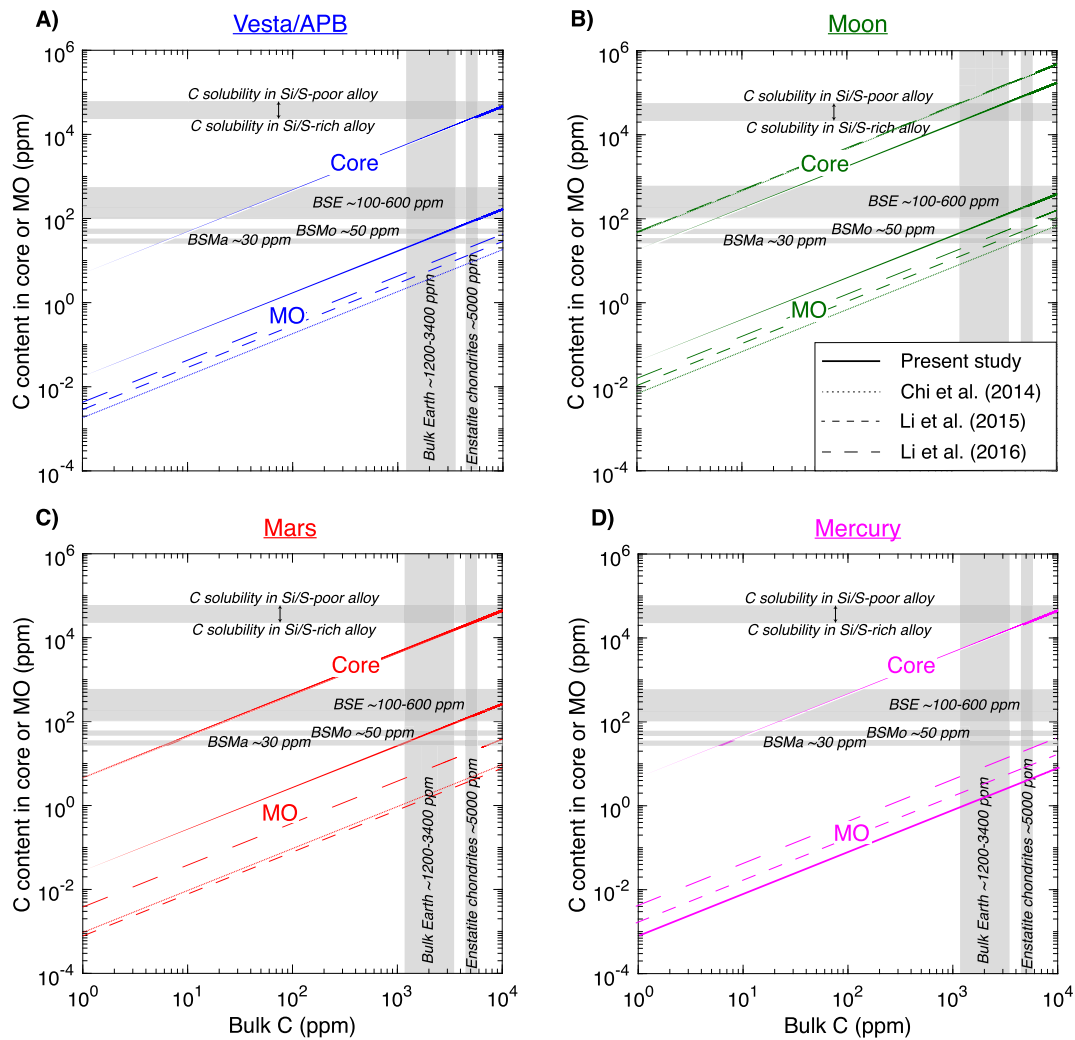


**Fig. 8.** C contents in the metallic cores and silicate magma oceans of **A)** Vesta/Angrite parent body, **B)** Moon, **C)** Mars, and **D)** Mercury as a function of bulk carbon contents involved in their core-mantle differentiation. Based on the estimates for the  $f_{O_2}$  conditions of core-mantle differentiation, the distribution is calculated based on the predicted  $D_{C}^{alloy/silicate}$  values for the most C-poor system explored in this study (blue lines in Fig. 7). Also plotted for comparison is the distribution of C based on the predicted  $D_{C}^{alloy/silicate}$  values from previous studies that generated C-rich (graphite saturated) alloys.  $P$ - $T$ - $X$  conditions of core-mantle differentiation as well as alloy/silicate mass ratios were compiled from previous studies (Rai and Van Westrenen, 2013; Steenstra et al., 2016a,b). Acronyms: BSE = Bulk Silicate Earth; BSMo = Bulk Silicate Moon; BSMa = Bulk Silicate Mars. Data sources: C solubility in Si/S-poor alloys – Chi et al. (2014) and Dasgupta et al. (2013); C solubility in Si/S-rich alloys – Grewal et al. (2019a,b), Li et al. (2016) and Tsuno et al. (2018); Bulk Silicate Earth C content – Hirschmann (2016) and Marty et al. (2020); Bulk Silicate Moon C content – Wetzal et al. (2015); Bulk Silicate Mars C content – Yoshizaki and McDonough (2020); Bulk Earth C content – based on the C content of bulk Earth containing 100–600 ppm and 0.4–1 wt.% C in its bulk silicate and core reservoirs, respectively (Dasgupta and Grewal, 2019; Hirschmann, 2018; Marty et al., 2020; Wood et al., 2013); C content of enstatite chondrites – Grady and Wright (2003).

than the values predicted by previous studies using C-rich systems. Whereas C contents of the cores broadly lie within the range of those predicted by previous studies. If enstatite chondrite-like C abundances ( $\sim 5000$  ppm) were available during core-mantle differentiation in these rocky bodies, then C contents in the MOs and cores were: Vesta/APB =  $\sim 80$  ppm and  $\sim 2$  wt.%, Moon =  $\sim 110$  ppm and  $\sim 5$ – $6$  wt.% (based on C solubility in graphite saturated alloys), and Mars =  $\sim 100$  ppm and  $\sim 2$  wt.% (Fig. 8A, B, C). On the other hand, if  $\sim 1200$ – $3400$  ppm C (based on the C content of bulk Earth containing 100–600 ppm and 0.4–1 wt.% C in its bulk silicate and core reservoirs, respectively (Dasgupta and Grewal, 2019; Hirschmann, 2018; Marty et al., 2020; Wood et al., 2013) was available during core-mantle differentiation, then the predicted C abundances in the MOs and cores were: Vesta/APB =  $\sim 20$ – $50$  ppm and  $\sim 0.5$ – $1.7$  wt.%, Moon =  $\sim 50$ – $100$  ppm and  $\sim 1$ – $5$  wt.%, and Mars =  $\sim 30$ – $90$  ppm and  $\sim 0.5$ – $1.5$  wt.% (Fig. 8A, B, C). These predicted C concentrations in the MOs lie well within the range of estimated C contents in the bulk silicate reservoirs of Moon ( $\sim 50$

ppm) and Mars ( $\sim 30$  ppm) (Wetzal et al., 2015; Yoshizaki and McDonough, 2020). This indicates that if bulk Earth like C contents were available, then the C inventory of the bulk silicate reservoirs of Vesta, APB, Moon, and Mars were set exclusively during core-mantle differentiation. In such a scenario, the contribution of late accretion events to the C budgets of the bulk silicate reservoirs of these bodies would be minimal. In conclusion, this study – in agreement with previous studies – predicts that core formation depletes C in the MOs of rocky bodies, but the extent of depletion may not be as severe as predicted earlier.

The alloy/silicate mass ratio during core-mantle differentiation in Mercury is uncertain due to the likely stripping of Mercury's primitive mantle during impacts (Helffrich et al., 2019). Assuming the present-day core/mantle mass ratio is broadly representative of the alloy/silicate mass ratio involved during its core-mantle differentiation, we can make first order predictions on the C abundances in MOs and cores of extremely reduced bodies like Mercury and aubrite parent body. For bulk Earth-like and enstatite

chondrite-like C abundances involved during core-mantle differentiation yields 1–3 ppm and 0.5–2 wt.% C in the resulting MO and core reservoirs, respectively, of Mercury (Fig. 8D). Implementing our  $D_C^{\text{alloy/silicate}}$  values to a single stage core-mantle differentiation scenario in Earth results in a relatively C-poor bulk silicate Earth (BSE) after core formation. This – along with the constraints on C/N and C/S ratio of the BSE – implies that a major portion of C inventory of the BSE was likely delivered via a differentiated impactor with a C-rich mantle towards the tail end of Earth's main accretion phase (Grewal et al., 2019b; Li et al., 2016; Tsuno et al., 2018). On the other hand, if  $D_C^{\text{alloy/silicate}}$  is lower for deeper MOs (as predicted by Blanchard et al. (2019) and Fischer et al. (2020)), then the C inventory of the BSE may be set during Earth's growth without requiring the accretion of a C-rich impactor. However, it is not possible to simultaneously reconcile the superchondritic C/N and chondritic C/S ratios of the present-day BSE using only a lesser siderophile behavior of C. This suggests that even though it may be possible to satisfy the present-day C inventory of BSE via accretion of C during Earth's main growth phase, accretion of C-rich impactors maybe necessary to simultaneously satisfy C/N and C/S ratios in the BSE (Grewal et al., 2019b; Hirschmann, 2016).

## 5. Concluding remarks

In this study we show that in graphite-undersaturated conditions – (1) at a fixed bulk C,  $D_C^{\text{alloy/silicate}}$  increases with a decrease in  $fO_2$  from IW–2.6 to IW–4.2 followed by drop at more reducing conditions, and (2) at a given  $fO_2$ ,  $D_C^{\text{alloy/silicate}}$  increases with increase in bulk C content of the system. C dissolution as anhydrous species ( $CO_3^{2-} + CO$ ) appears to control the variation of  $D_C^{\text{alloy/silicate}}$  as a function of  $fO_2$  for mafic-ultramafic, water-poor silicate melts in graphite-undersaturated conditions at  $>IW-4.2$ ; below IW–4.2, hydrated C species (C–H) in silicate melts seem to affect  $D_C^{\text{alloy/silicate}}$ .  $D_C^{\text{alloy/silicate}}$  varies with bulk C because C partitioning between alloy and silicate melts shows non-Henrian behavior. This is due to an increase in  $\gamma_C^{\text{alloy melt}}$  with increasing C content of the alloy, with graphite-saturated alloys having the highest  $\gamma_C^{\text{alloy melt}}$  values at a given  $fO_2$ . Therefore, in addition to other thermodynamic variables,  $D_C^{\text{alloy/silicate}}$  is strongly dependent on the C content available during core-mantle differentiation. As rocky bodies in the inner Solar System likely accreted thermally processed C-poor materials, graphite-undersaturated experiments of this study (having water-poor, mafic-ultramafic silicate melts) more realistically simulate C fractionation during core-mantle differentiation in such bodies. In agreement with previous experimental studies relevant for shallow MOs ( $\leq 8$  GPa) (except for Fichtner et al. (2021) and Malavergne et al. (2019)), our data shows that C is moderately siderophile during core-mantle differentiation. But the overall range of predicted  $D_C^{\text{alloy/silicate}}$  values, especially at moderately oxidizing core forming conditions, i.e., between IW–2 and IW, is lower by as much as an order of magnitude in comparison with previous estimates. We conclude that sequestration of C into the metallic cores did play a crucial role in depleting C from the bulk silicate reservoirs of rocky protoplanets and planets in the inner Solar System; however, the extent of depletion was less severe than previously predicted.

## CRedit authorship contribution statement

**Damanveer S. Grewal:** Conceptualization, Funding acquisition, Investigation, Methodology, Validation, Writing – original draft. **Rajdeep Dasgupta:** Conceptualization, Funding acquisition, Methodology, Resources, Supervision, Validation, Writing – review & editing. **Sanath Aithala:** Investigation.

## Declaration of competing interest

The authors declare that they have no known competing financial interests or personal relationships that could have appeared to influence the work reported in this paper.

## Acknowledgements

We thank Celia Dalou, Bernard Wood, and three anonymous reviewers for their comments which significantly improved the manuscript. We also thank James Badro for handling the manuscript. Gelu Costin and Brian Monteleone are acknowledged for their help with the electron and ion microprobe analyses, respectively. D.S.G. was supported by a NASA FINESST grant 80NSSC19K1538 and a Lodieska Stockbridge Vaughn Fellowship by Rice University. Additional support came from NASA grants 80NSSC18K0828 and 80NSSC18K1314 to R.D.

## Appendix A. Supplementary material

Supplementary material related to this article can be found online at <https://doi.org/10.1016/j.epsl.2021.117090>.

## References

- Armstrong, L.S., Hirschmann, M.M., Stanley, B.D., Falksen, E.G., Jacobsen, S.D., 2015. Speciation and solubility of reduced C–O–H–N volatiles in mafic melt: implications for volcanism, atmospheric evolution, and deep volatile cycles in the terrestrial planets. *Geochim. Cosmochim. Acta* 171, 283–302. <https://doi.org/10.1016/j.gca.2015.07.007>.
- Badro, J., Cote, A.S., Brodholt, J.P., 2014. A seismologically consistent compositional model of Earth's core. *Proc. Natl. Acad. Sci.* 111, 7542–7545. <https://doi.org/10.1073/pnas.1316708111>.
- Badro, J., Brodholt, J.P., Piet, H., Siebert, J., Ryerson, F.J., 2015. Core formation and core composition from coupled geochemical and geophysical constraints. *Proc. Natl. Acad. Sci.* 112, 12310–12314. <https://doi.org/10.1073/pnas.1505672112>.
- Bajgain, S., Mookherjee, M., Dasgupta, R., 2021. Earth's core could be the largest terrestrial carbon reservoir. *Commun. Earth Environ.* <https://doi.org/10.1038/s43247-021-00222-7>.
- Beattie, P., 1993. On the occurrence of apparent non-Henry's Law behaviour in experimental partitioning studies. *Geochim. Cosmochim. Acta* 57, 47–55. [https://doi.org/10.1016/0016-7037\(93\)90467-B](https://doi.org/10.1016/0016-7037(93)90467-B).
- Blanchard, I., Jennings, E., Franchi, I., Zhao, X., Petitgirard, S., Miyajima, N., Jacobson, S.A., Rubie, D., 2019. The fate of carbon during Earth's core-mantle differentiation. *EarthArXiv*, 1–33. <https://doi.org/10.31222/osf.io/9t7ps>.
- Bouchard, D., Bale, C.W., 1995. Simultaneous optimization of thermochemical data for liquid iron alloys containing C, N, Ti, Si, Mn, S, and P. *Metall. Mater. Trans. B* 26, 467–484. <https://doi.org/10.1007/BF02653863>.
- Brennan, M.C., Fischer, R.A., Irving, J.C.E., 2020. Core formation and geophysical properties of Mars. *Earth Planet. Sci. Lett.* 530, 115923. <https://doi.org/10.1016/j.epsl.2019.115923>.
- Cartier, C., Wood, B.J., 2019. The role of reducing conditions in building Mercury. *Elements* 15, 39–45. <https://doi.org/10.2138/gselements.15.1.39>.
- Chi, H., Dasgupta, R., Duncan, M.S., Shimizu, N., 2014. Partitioning of carbon between Fe-rich alloy melt and silicate melt in a magma ocean – implications for the abundance and origin of volatiles in Earth, Mars, and the moon. *Geochim. Cosmochim. Acta* 139, 447–471. <https://doi.org/10.1016/j.gca.2014.04.046>.
- Dalou, C., Hirschmann, M.M., von der Handt, A., Mosenfelder, J., Armstrong, L.S., 2017. Nitrogen and carbon fractionation during core-mantle differentiation at shallow depth. *Earth Planet. Sci. Lett.* 458, 141–151. <https://doi.org/10.1016/j.epsl.2016.10.026>.
- Dalou, C., Hirschmann, M.M., Jacobsen, S.D., Le Losq, C., 2019. Raman spectroscopy study of C–O–H–N speciation in reduced basaltic glasses: implications for reduced planetary mantles. *Geochim. Cosmochim. Acta* 265, 32–47. <https://doi.org/10.1016/j.gca.2019.08.029>.
- Dasgupta, R., Grewal, D.S., 2019. Origin and early differentiation of carbon and associated life-essential volatile elements on Earth. *Deep carbon*. In: Orcutt, B., Daniel, I., Dasgupta, R. (Eds.), *Deep Carbon: Past to Present*. Cambridge Univ. Press, Cambridge, pp. 4–39.
- Dasgupta, R., Chi, H., Shimizu, N., Buono, A.S., Walker, D., 2013. Carbon solution and partitioning between metallic and silicate melts in a shallow magma ocean: implications for the origin and distribution of terrestrial carbon. *Geochim. Cosmochim. Acta* 102, 191–212. <https://doi.org/10.1016/j.gca.2012.10.011>.
- Dauphas, N., 2017. The isotopic nature of the Earth's accreting material through time. *Nature* 541, 521–524. <https://doi.org/10.1038/nature20830>.



- Davis, F.A., Tangeman, J.A., Tenner, T.J., Hirschmann, M.M., 2009. The composition of KLB-1 peridotite. *Am. Mineral.* 94, 176–180. <https://doi.org/10.2138/am.2009.2984>.
- Duncan, M.S., Dasgupta, R., Tsuno, K., 2017. Experimental determination of CO<sub>2</sub> content at graphite saturation along a natural basalt-peridotite melt join: implications for the fate of carbon in terrestrial magma oceans. *Earth Planet. Sci. Lett.* 466, 115–128. <https://doi.org/10.1016/j.epsl.2017.03.008>.
- Eguchi, J., Dasgupta, R., 2018. A CO<sub>2</sub> solubility model for silicate melts from fluid saturation to graphite or diamond saturation. *Chem. Geol.* 487, 23–38. <https://doi.org/10.1016/j.chemgeo.2018.04.012>.
- Fichtner, C.E., Schmidt, M.W., Liebske, C., Bouvier, A.-S., Baumgartner, L.P., 2021. Carbon partitioning between metal and silicate melts during Earth accretion. *Earth Planet. Sci. Lett.* 554, 116659. <https://doi.org/10.1016/j.epsl.2020.116659>.
- Fischer, R.A., Cottrell, E., Hauri, E., Lee, K.K.M., Le Voyer, M., 2020. The carbon content of Earth and its core. *Proc. Natl. Acad. Sci.* 201919930. <https://doi.org/10.1073/pnas.1919930117>.
- Grady, M.M., Wright, I.P., 2003. Elemental and isotopic abundances of carbon and nitrogen in meteorites. *Space Sci. Rev.* <https://doi.org/10.1023/A:1024645906350>.
- Grewal, D.S., Dasgupta, R., Holmes, A.K., Costin, G., Li, Y., Tsuno, K., 2019a. The fate of nitrogen during core-mantle separation on Earth. *Geochim. Cosmochim. Acta* 251, 87–115. <https://doi.org/10.1016/j.gca.2019.02.009>.
- Grewal, D.S., Dasgupta, R., Sun, C., Tsuno, K., Costin, G., 2019b. Delivery of carbon, nitrogen, and sulfur to the silicate Earth by a giant impact. *Sci. Adv.* 5, eaau3669. <https://doi.org/10.1126/sciadv.aau3669>.
- Grewal, D.S., Dasgupta, R., Farnell, A., 2020. The speciation of carbon, nitrogen, and water in magma oceans and its effect on volatile partitioning between major reservoirs of the Solar System rocky bodies. *Geochim. Cosmochim. Acta* 280, 281–301. <https://doi.org/10.1016/j.gca.2020.04.023>.
- Grewal, D.S., Dasgupta, R., Hough, T., Farnell, A., 2021a. Rates of protoplanetary accretion and differentiation set nitrogen budget of rocky planets. *Nat. Geosci.* 14, 369–376. <https://doi.org/10.1038/s41561-021-00733-0>.
- Grewal, D.S., Dasgupta, R., Marty, B., 2021b. A very early origin of isotopically distinct nitrogen in inner Solar System protoplanets. *Nat. Astron.* 5, 356–364. <https://doi.org/10.1038/s41550-020-01283-y>.
- Helfrich, G., Brasser, R., Shahar, A., 2019. The chemical case for Mercury mantle stripping. *Prog. Earth Planet. Sci.* 6, 66. <https://doi.org/10.1186/s40645-019-0312-z>.
- Hirschmann, M.M., 2012. Magma ocean influence on early atmosphere mass and composition. *Earth Planet. Sci. Lett.* 341–344, 48–57. <https://doi.org/10.1016/j.epsl.2012.06.015>.
- Hirschmann, M.M., 2016. Constraints on the early delivery and fractionation of Earth's major volatiles from C/H, C/N, and C/S ratios. *Am. Mineral.* 101, 540–553. <https://doi.org/10.2138/am-2016-5452>.
- Hirschmann, M.M., 2018. Comparative deep Earth volatile cycles: the case for C recycling from exosphere/mantle fractionation of major (H<sub>2</sub>O, C, N) volatiles and from H<sub>2</sub>O/Ce, CO<sub>2</sub>/Ba, and CO<sub>2</sub>/Nb exosphere ratios. *Earth Planet. Sci. Lett.* 502, 262–273. <https://doi.org/10.1016/j.epsl.2018.08.023>.
- Hirschmann, M.M., Bergin, E.A., Blake, G.A., Ciesla, F.J., Li, J., 2021. Early volatile depletion on planetesimals inferred from C–S systematics of iron meteorite parent bodies. *Proc. Natl. Acad. Sci.* 118, e2026779118. <https://doi.org/10.1073/pnas.2026779118>.
- Keppler, H., Golabek, G., 2019. Graphite floatation on a magma ocean and the fate of carbon during core formation. *Geochem. Perspect. Lett.* 11, 12–17. <https://doi.org/10.7185/geochemlet.1918>.
- Kilburn, M.R., Wood, B.J., 1997. Metal–silicate partitioning and the incompatibility of S and Si during core formation. *Earth Planet. Sci. Lett.* 152, 139–148. [https://doi.org/10.1016/S0012-821X\(97\)00125-8](https://doi.org/10.1016/S0012-821X(97)00125-8).
- Kuramoto, K., Matsui, T., 1996. Partitioning of H and C between the mantle and core during the core formation in the Earth: its implications for the atmospheric evolution and redox state of early mantle. *J. Geophys. Res. E, Planets* 101, 14909–14932. <https://doi.org/10.1029/96JE00940>.
- Kuwahara, H., Itoh, S., Nakada, R., Irifune, T., 2019. The effects of carbon concentration and silicate composition on the metal–silicate partitioning of carbon in a shallow magma ocean. *Geophys. Res. Lett.* 46, 9422–9429. <https://doi.org/10.1029/2019GL084254>.
- Kuwahara, H., Itoh, S., Suzumura, A., Nakada, R., Irifune, T., 2021. Nearly carbon-saturated magma oceans in planetary embryos during core formation. *Geophys. Res. Lett.* 1–25. <https://doi.org/10.1029/2021GL092389>.
- Li, Y., Dasgupta, R., Tsuno, K., 2015. The effects of sulfur, silicon, water, and oxygen fugacity on carbon solubility and partitioning in Fe-rich alloy and silicate melt systems at 3 GPa and 1600 °C: implications for core–mantle differentiation and degassing of magma oceans and reduced planet. *Earth Planet. Sci. Lett.* 415, 54–66. <https://doi.org/10.1016/j.epsl.2015.01.017>.
- Li, Y., Dasgupta, R., Tsuno, K., Monteleone, B., Shimizu, N., 2016. Carbon and sulfur budget of the silicate Earth explained by accretion of differentiated planetary embryos. *Nat. Geosci.* 9, 781–785. <https://doi.org/10.1038/ng eo2801>.
- Li, Y., Dasgupta, R., Tsuno, K., 2017. Carbon contents in reduced basalts at graphite saturation: implications for the degassing of Mars, Mercury, and the Moon. *J. Geophys. Res., Planets* 122, 1300–1320. <https://doi.org/10.1002/2017JE005289>.
- Malavergne, V., Bureau, H., Raepsaet, C., Gaillard, F., Poncet, M., Surblé, S., Sifré, D., Shcheka, S., Fourdrin, C., Deldicque, D., Khodja, H., 2019. Experimental constraints on the fate of H and C during planetary core–mantle differentiation. Implications for the Earth. *Icarus* 321, 473–485. <https://doi.org/10.1016/j.icarus.2018.11.027>.
- Marty, B., Almayrac, M., Barry, P.H., Bekaert, D.V., Broadley, M.W., Byrne, D.J., Ballentine, C.J., Caracausi, A., 2020. An evaluation of the C/N ratio of the mantle from natural CO<sub>2</sub>-rich gas analysis: geochemical and cosmochemical implications. *Earth Planet. Sci. Lett.* 551, 116574. <https://doi.org/10.1016/j.epsl.2020.116574>.
- Nittler, L.R., Chabot, N.L., Grove, T.L., Peplowski, P.N., 2019. The chemical composition of Mercury. In: Solomon, Sean C., Nittler, Larry R., Anderson, B.J. (Eds.), *Mercury the View After MESSENGER*. Cambridge University Press, pp. 30–51.
- Piani, L., Marrocchi, Y., Rigaudier, T., Vacher, L.G., Thomassin, D., Marty, B., 2020. Earth's water may have been inherited from material similar to enstatite chondrite meteorites. *Science* 80 (369), 1110–1113. <https://doi.org/10.1126/science.aba1948>.
- Rai, N., Van Westrenen, W., 2013. Core–mantle differentiation in Mars. *J. Geophys. Res. E, Planets* 118, 1195–1203. <https://doi.org/10.1002/jgre.20093>.
- Righter, K., Sutton, S.R., Danielson, L., Pando, K., Newville, M., 2016. Redox variations in the inner solar system with new constraints from vanadium XANES in spinels. *Am. Mineral.* <https://doi.org/10.2138/am-2016-5638>.
- Stanley, B.D., Hirschmann, M.M., Withers, A.C., 2014. Solubility of COH volatiles in graphite-saturated martian basalts. *Geochim. Cosmochim. Acta* 129, 54–76. <https://doi.org/10.1016/j.gca.2013.12.013>.
- Steenstra, E.S., Knibbe, J.S., Rai, N., van Westrenen, W., 2016a. Constraints on core formation in Vesta from metal–silicate partitioning of siderophile elements. *Geochim. Cosmochim. Acta* 177, 48–61. <https://doi.org/10.1016/j.gca.2016.01.002>.
- Steenstra, E.S., Rai, N., Knibbe, J.S., Lin, Y.H., van Westrenen, W., 2016b. New geochemical models of core formation in the Moon from metal–silicate partitioning of 15 siderophile elements. *Earth Planet. Sci. Lett.* 441, 1–9. <https://doi.org/10.1016/j.epsl.2016.02.028>.
- Taylor, S.R., 1982. *Planetary Science: A Lunar Perspective*. Lunar and Planetary Institute, Houston.
- Toplis, M.J., Mizzon, H., Monnereau, M., Forni, O., McSweeney, H.Y., Mittlefehldt, D.W., McCoy, T.J., Prettyman, T.H., De Sanctis, M.C., Raymond, C.A., Russell, C.T., 2013. Chondritic models of 4 Vesta: implications for geochemical and geophysical properties. *Meteorit. Planet. Sci.* 48, 2300–2315. <https://doi.org/10.1111/maps.12195>.
- Tsuno, K., Dasgupta, R., 2011. Melting phase relation of nominally anhydrous, carbonated pelitic-eclogite at 2.5–3.0 GPa and deep cycling of sedimentary carbon. *Contrib. Mineral. Petrol.* 161, 743–763. <https://doi.org/10.1007/s00410-010-0560-9>.
- Tsuno, K., Grewal, D.S., Dasgupta, R., 2018. Core–mantle fractionation of carbon in Earth and Mars: the effects of sulfur. *Geochim. Cosmochim. Acta* 238, 477–495. <https://doi.org/10.1016/j.gca.2018.07.010>.
- Wang, C., Hiram, J., Nagasaka, T., Ban-Ya, S., 1991. Phase equilibria of liquid Fe–S–C ternary system. *ISIJ Int.* 31, 1292–1299. <https://doi.org/10.2355/isijinternational.31.1292>.
- Wetzel, D.T., Rutherford, M.J., Jacobsen, S.D., Hauri, E.H., Saal, A.E., 2013. Degassing of reduced carbon from planetary basalts. *Proc. Natl. Acad. Sci.* 110, 8010–8013. <https://doi.org/10.1073/pnas.1219266110>.
- Wetzel, D.T., Hauri, E.H., Saal, A.E., Rutherford, M.J., 2015. Carbon content and degassing history of the lunar volcanic glasses. *Nat. Geosci.* 8, 755–758. <https://doi.org/10.1038/ng eo2511>.
- Wood, B.J., 1993. Carbon in the core. *Earth Planet. Sci. Lett.* 117, 593–607. [https://doi.org/10.1016/0012-821X\(93\)90105-1](https://doi.org/10.1016/0012-821X(93)90105-1).
- Wood, B.J., Li, J., Shahar, A., 2013. Carbon in the core: its influence on the properties of core and mantle. *Rev. Mineral. Geochem.* 75, 231–250. <https://doi.org/10.2138/rmg.2013.75.8>.
- Yoshioka, T., McCammon, C., Shcheka, S., Keppler, H., 2015. The speciation of carbon monoxide in silicate melts and glasses. *Am. Mineral.* 100, 1641–1644. <https://doi.org/10.2138/am-2015-5315>.
- Yoshioka, T., Nakashima, D., Nakamura, T., Shcheka, S., Keppler, H., 2019. Carbon solubility in silicate melts in equilibrium with a CO–CO<sub>2</sub> gas phase and graphite. *Geochim. Cosmochim. Acta*. <https://doi.org/10.1016/j.gca.2019.06.007>.
- Yoshizaki, T., McDonough, W.F., 2020. The composition of Mars. *Geochim. Cosmochim. Acta* 273, 137–162. <https://doi.org/10.1016/j.gca.2020.01.011>.